Supporting Information

Efficient electrodynamic stripping for 12-inch wafer-scale freestanding ferroelectric membranes

Hangren Li[1,#], Jie Tu[1,#], Siyuan Du[1,#], Guoqiang Xi[1,2], Chen Liu[3], Yue-Wen Fang[4], Shuai Xu[5], Jia-Han Zhang[6], Enqi Sun[7], Shunli Ouyang[8], Xudong Liu[1], Longyuan Shi[1], Xiuqiao Liu[1], Dongxing Zheng[3], Lei Guo[9], Xixiang Zhang[3], Kuijuan Jin[5], Jianjun Tian[1], Linxing Zhang[1,10], Xianran Xing[10]**

1. *Institute for Advanced Materials Technology, University of Science and Technology Beijing, Beijing 100083, China*
2. *State Key Laboratory of Radio Frequency Heterogeneous Integration (Shenzhen University), College of Electronics and Information Engineering, Shenzhen University, Shenzhen 518060, China*
3. *Physical Science and Engineering Division, King Abdullah University of Science and Technology (KAUST), Thuwal 23955–6900, Saudi Arabia*
4. *Centro de Física de Materiales (CSIC-UPV/EHU), Manuel de Lardizabal Pasealekua 5, 20018 Donostia/San Sebastián, Spain*
5. *Beijing National Laboratory for Condensed Matter Physics, Institute of Physics, Chinese Academy of Sciences, Beijing 100190, China*
6. *Electronic-Photonic Smart Sensing Device R&D Team, Inner Mongolia Key Laboratory of Intelligent Communication and Sensing and Signal Processing, School of Electronic Information Engineering, Inner Mongolia University, Hohhot 010021, China*
7. *School of Mathematics and Physics, University of Science and Technology Beijing, Beijing 100083, China*
8. *Guangdong Provincial Key Laboratory of Nanhai Microbial Mineralization Technology and Application, Guangzhou Maritime University, Guangzhou 510725, China*
9. *State Key Laboratory of Advanced Metallurgy, University of Science and Technology Beijing, Beijing 100083, China*
10. *Institute of Solid State Chemistry, University of Science and Technology Beijing, Beijing 100083, China*

** Correspondence to: linxingzhang@ustb.edu.cn, xing@ustb.edu.cn*

[#] These authors contributed equally to this work

Methods

Preparation of sacrificial and target films

1.1 $LaNiO_3$

The required amount of Lanthanum nitrate hexahydrate ($La(NO_3)_3 \cdot 6H_2O$, aladdin, 99%), Nickel(II) acetate tetrahydrate ($NiC_4H_6O_4 \cdot 4H_2O$, aladdin, 99.9%)is dissolved in 2-Methoxyethanol($C_3H_8O_2$, aladdin, 99.5%). Then, the mixed solvent was heated and stirred on a 75 ℃ hot platform for 2 hours to obtain a transparent precursor solution. Finally, the solvent is left to stand at room temperature for filtration.

The precursor solution is spin coated on a 10×10 mm^2 STO or LAO substrate and rotated at a high speed of 5000 rpm for 30 seconds. On the hot table, the water in the film was removed by heating at 120 °C for 3 minutes, and the organic solvent was removed by heating at 350 °C for 10 minutes. Subsequently, the $LaNiO_3$ sample was subjected to annealing in a rapid annealing furnace 650 °C-750 °C for approximately 5 minutes.

1.2 $PbZrO_3$

The required amount of Lead nitrate ($Pb(NO_3)_2$, aladdin, 99.999%) and Nickel(II) acetate tetrahydrate ($NiC_4H_6O_4 \cdot 4H_2O$, aladdin, 99.9%) is dissolved in 2-Methoxyethanol ($C_3H_8O_2$, aladdin, 99.5%), There was 10% too much lead. Then, the mixed solvent was heated and stirred on a 75 ℃ hot platform for 2 hours to obtain a transparent green precursor solution. Finally, the solvent is left to stand at room temperature for filtration.

The precursor solution is spin coated on a 10×10 mm^2 LNO/STO or LNO/ LAO substrate and rotated at a high speed of 5000 rpm for 30 seconds. On the hot table, the water in the film was removed by heating at 120 °C for 3 minutes, and the organic solvent was removed by heating at 350 °C for 10 minutes. Subsequently, the PZO sample was subjected to annealing in a hostler furnace 700°C for approximately 30 minutes.

1.3 $SrTiO_3$

The required amount of Strontium acetate ($C_4H_6O_4Sr$, mackun, 99%) and Titanium

(IV) oxide acetylacetonate ($C_{10}H_{14}O_5Ti$, aladdin, 98%) is dissolved in acetic acid, then 2, 4-pentanedione is added. A solution with a metal ion concentration of 0.1 mol/L is obtained, in which the ratio of acetic acid to 2, 4-pentanedione is 3:2. Finally, the mixed solvent was heated on a hot table at 75 °C for 2 hours to obtain a transparent precursor solution.

The precursor solution is spin coated on a 10×10 mm^2 LNO/LAO substrate and rotated at a high speed of 5000 rpm for 30 seconds. On the hot table, the water in the film was removed by heating at 120 °C for 3 minutes, and the organic solvent was removed by heating at 350 °C for 10 minutes. Subsequently, the STO sample was subjected to annealing in a hostler furnace 900°C for approximately 30 minutes.

1.4 $LaAlO_3$

The required amount of Lanthanum nitrate hexahydrate ($La(NO_3)_3 \cdot 6H_2O$, aladdin, 99%) and Aluminum triacetylacetone ($C_{15}H_{21}O_6Al$, aladdin, 99.999%) is dissolved in acetic acid, then 2, 4-pentanedione is added. A solution with a metal ion concentration of 0.1 mol/L is obtained, in which the ratio of acetic acid to 2, 4-pentanedione is 3:2. Finally, the mixed solvent was heated on a hot table at 75 °C for 2 hours to obtain a transparent precursor solution.

The precursor solution is spin coated on a 10×10 mm^2 LNO/STO substrate and rotated at a high speed of 5000 rpm for 30 seconds. On the hot table, the water in the film was removed by heating at 120 °C for 3 minutes, and the organic solvent was removed by heating at 300 °C for 3 minutes. Subsequently, the LAO sample was subjected to annealing in a hostler furnace 1050°C for approximately 20 minutes.

1.5 $YMnO_3$

The required amount of Yttrium nitrate hexahydrate ($Y(NO_3)_3 \cdot 6H_2O$, Macklin, 99.9%) and Manganese acetate ($(CH3COO)_2Mn$, Alfa, 98%) is dissolved in acetic acid, then 2, 4-pentanedione is added. A solution with a metal ion concentration of 0.2 mol/L is obtained, in which the ratio of acetic acid to 2, 4-pentanedione is 3:2. Finally, the mixed solvent was heated on a hot table at 75 °C for 2 hours to obtain a transparent brown green precursor solution.

The precursor solution is spin coated on a 10×10 mm^2 LNO/STO substrate and rotated at a high speed of 5000 rpm for 30 seconds. On the hot table, the water in the

film was removed by heating at 120 °C for 3 minutes, and the organic solvent was removed by heating at 300 °C for 3 minutes. Subsequently, the YMO sample was subjected to annealing in a hostler furnace 800°C for approximately 20 minutes.

1.6 $BiFeO_3$

The chemicals used in the experiment were bismuth oxide (Bi_2O_3, 99.9%, Aladdin) and iron oxide (Fe_2O_3, 99.9%, Aladdin). Polyvinyl alcohol was used as the binder for the target. The prepared target was sintered at 750°C for 2 hours. BFO films were fabricated by radio-frequency (RF) magnetron sputtering (VJC-300, Beijing VNANO Vacuum Technology CO, Ltd) on a LNO/STO substrate, which was heated at 500 °C and the cavity was vacuumized below 2×10^{-5} Torr. A total of 5.5 sccm of a mixture of nitrogen (45.5%) and oxygen (54.5%) was pumped into the chamber to maintain a pressure of 0.4 Pa. Continuous 2.5 hours of high RF power (90 W) sputtering and 0.5 hours of low RF (60 W) sputtering were performed. Finally, they were annealed under a full oxygen atmosphere for 20 minutes.

1.7 Description of electrical stripping

Using 304 stainless steel clip, it can grasp a corner of the LAO, YMO, BFO, PZO or STO film. This clip is affixed to the anode of the current source. Subsequently, the cathode of the current source is then connected to the carbon rod, which should then be immersed in an acetic acid solution. The applied current is 5 amperes, with the voltage of 10-25 volts for LAO, YMO, PZO and STO films and 1 volt for BFO film.

Characterization methods

2.1 Density Functional Theory Calculations

In the Density Functional Theory (DFT) calculations of the interface between the acetic acid and sacrificial layer, the projector augmented wave (PAW) method [33] as implemented in the Vienna Ab initio Simulation Package (VASP) [34] was employed. The Perdew-Burke-Ernzerhof (PBE) formulation was used for the exchange-correlation interactions. The calculations were performed in a spin-polarized manner. The cut-off

energy of the plane-wave basis is set at 520 eV and the Brillouin zone integration was performed on a 2x2x1 *k*-points grid. The geometry structures were relaxed with a force threshold of 0.02 eV/Å. The unit cell of $LaNiO_3$ is expanded by a factor of 4x4x2, the 110 surface is cleaved, and a surface model is constructed with La as the terminal. The adsorption energy is calculated by subtracting the energies of the surface and the adsorbate from the energy of the adsorbed state.

Molecular Dynamic Simulation (MD) selected Materials studio 2019 (Forcite module) to simulate A droplet with A diameter of 15 A under 0 and 0.5 eV/Å/e electric fields in the NVT ensemble (Berendsen). Affinity behavior on $LaNiO_3$ (13x13x4) interface. And the affinity behavior of droplets forming channels in the center.

For finite element analysis, we used the solid-flow coupling method and COMSOL Multiphysics (6.3) software to deeply analyze the effects of liquid diffusion velocity and decomposition velocity on the stress of the target layer. Under the target layer with a thickness of 100 nm, the decomposition channels with a thickness of 5 nm and 20 nm were constructed respectively, and the total length of the channels was set to 500 nm. By adjusting the inlet and outlet velocity of laminar flow, the change of diffusion velocity and decomposition velocity of different liquids was simulated. The simulation time was 4.65 s. In the process of model construction, the free triangle refinement mesh is used to divide the model to ensure the accuracy of the simulation results. In the simulation process, we used both laminar flow module and solid mechanics module. The density of the target layer material is assumed to be 1000 kg/m^3, Poisson's ratio is 0.4, and Young's modulus is 1 MPa. The density and dynamic viscosity of the flowing liquid are 1000kg/m^3 and 1Pa·s, respectively. Finally, the transient solver MUMPS was used to solve the model to obtain detailed simulation data and provide strong support for the subsequent stress analysis.

2.2 Current vs. time curve

Electrochemical workstation (Shanghai Chenhua Instrument Co., LTD.) was used to test the electrochemical decomposition process of LNO. Acetic acid solution (10%)

was selected as the electrolyte, and the decomposition time was tested respectively at 1A and 0.1 V, 2 V, 5 V, and10 V, respectively.

2.3 X-ray related diffraction

The structure and orientation of the thin films were investigated via synchrotron XRD, XRR, and RSM measurements, which were conducted at the Diffuse X-ray Scattering Station of the Beijing Synchrotron Radiation Facility (BSRF), Beamline 1W1A.

The thickness of thin film can be determined by the angular distance of two consecutive maxima in XRR. And the thinner the thin film, the larger the oscillation period. We have roughly calculated the thickness of the thin film according to Equation: $d = \lambda/2\Delta\theta$ where d is the thickness of the thin film, λ is the x-ray wavelength and λ = 1.5466 Å, $\Delta\theta$ is the period of the XRR stripes. XRR is usually correlated with the surface flatness and roughness of the film, so XRR can also prove that the film has a high-quality surface.

2.4 UV spectra

The ultraviolet-visible absorption spectra of the sacrificial layer (LNO, LCO, and LFO) were measured with a UV-Vis T10 spectrophotometer.

2.5 Optical photograph

The sample that was transferred was examined using a three-ocular monocular metallographic microscope (Cb-15100).

2.6 Ferroelectric hysteresis loop

For macroscopic ferroelectric measurements, circular top Pt electrodes with a diameter of 50 μm and a thickness of about 20 nm were deposited by magnetron sputtering. The ferroelectric hysteresis loops of the films were studied using TF-Analyzer 3000 (aixACCT).

2.7 Transmission election microscope

TEM experiments were performed with FEI Titan Themes Cubed G2 300 (Cs Probe) TEM at 300 kV. The noise in the HAADF-STEM images was reduced by using a Gaussian Filter in the Velox software.

2.8 Piezoresponse force microscopy

The piezoresponse force microscopy (PFM) is performed by Asylum Research MFP-3D-Infinity with Olympus AC240TM Pt/Ti coated silicon cantilevers (Asylum Research, USA).

2.9 Second harmonic generation

The incident laser beam for the SHG measurements was generated by a Spectra Physics Maitai SP Ti: Sapphire oscillator whose central wavelength is 800 nm and repetition frequency are 82 MHz. The incident power was fixed at 50 mW and focused on the sample surface with a diameter of ~100 μm. The *p*-out configurations were adopted during measurement, which denote the arrangements where the analyzer polarization is parallel to the plane of incident light field. The polarization direction φ of the incident light field is adjusted by the rotation of the λ/2 waveplate driven by a rotating motor.

2.10 Piezoelectric sensor test

A linear motor is used as a tool to adjust the curvature. The $PbZrO_3$ and PDMS films are horizontally fixed on the fixed end of the linear motor. One end of the two copper wires is connected to the two Pt electrodes, and the other end is connected to the positive and negative electrodes of the digital signal collector respectively (Keithley 6514, Tektronix/Fortive), which is used to read the voltage signal generated when the $PbZrO_3$ film is bent. The distance between the fixed end and the moving end of the linear motor is adjusted to make the film produce different bending angles, and the voltage signal of $PbZrO_3$ film at different bending angles is obtained through the periodic movement of the linear motor.

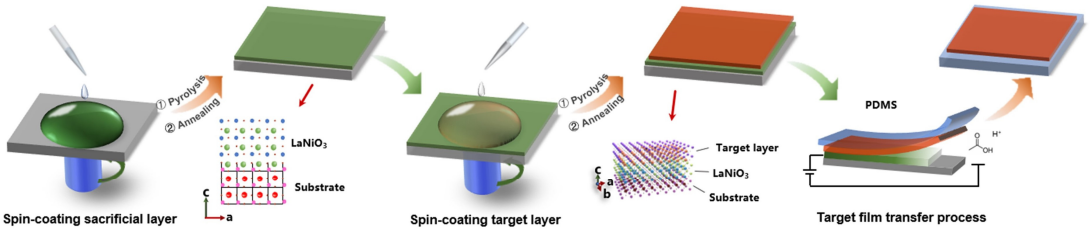

Extended Data Fig. 1 Schematic diagram of the transferred strategy after chemical preparation of LNO sacrificial layer and electrodynamic decomposition of sacrificial layer.

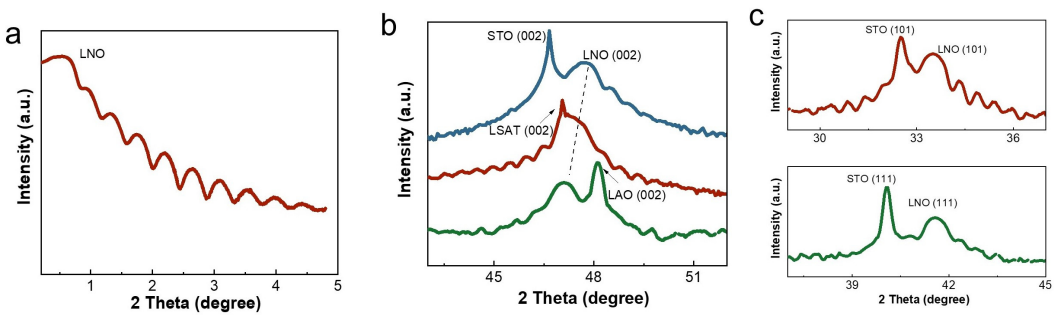

Extended Data Fig. 2 Crystal structure of LNO sacrificial layer. (a) Synchrotron-based XRR patterns of LNO sacrificial layers. **(b)** XRD patterns of LNO sacrificial layer around (002) peaks on STO, LSAT, and LAO substrates. **(c)** XRD patterns of LNO sacrificial layer on (101) and (111)-orientated STO substrates.

The LNO sacrificial layer can be also epitaxially grown on single-crystal substrates with varying lattice constants, such as (La,Sr)(Al,Ta)O_3 (LSAT) and LAO (Extended Data Fig. 2b). As the in-plane strain transitions from tensile strain of STO to the compressive strain of LAO, the out-of-plane lattice constant of LNO correspondingly increases, consistent with the expected Poisson effect. Furthermore, the epitaxial growth of La-based sacrificial layers on STO substrates with different orientations, including (101) and (111), is feasible (Extended Data Fig. 2c). This indicates the high lattice compatibility and stability of the La-based sacrificial layer, rendering them ideal for freestanding perovskite film research across various lattices and orientations.

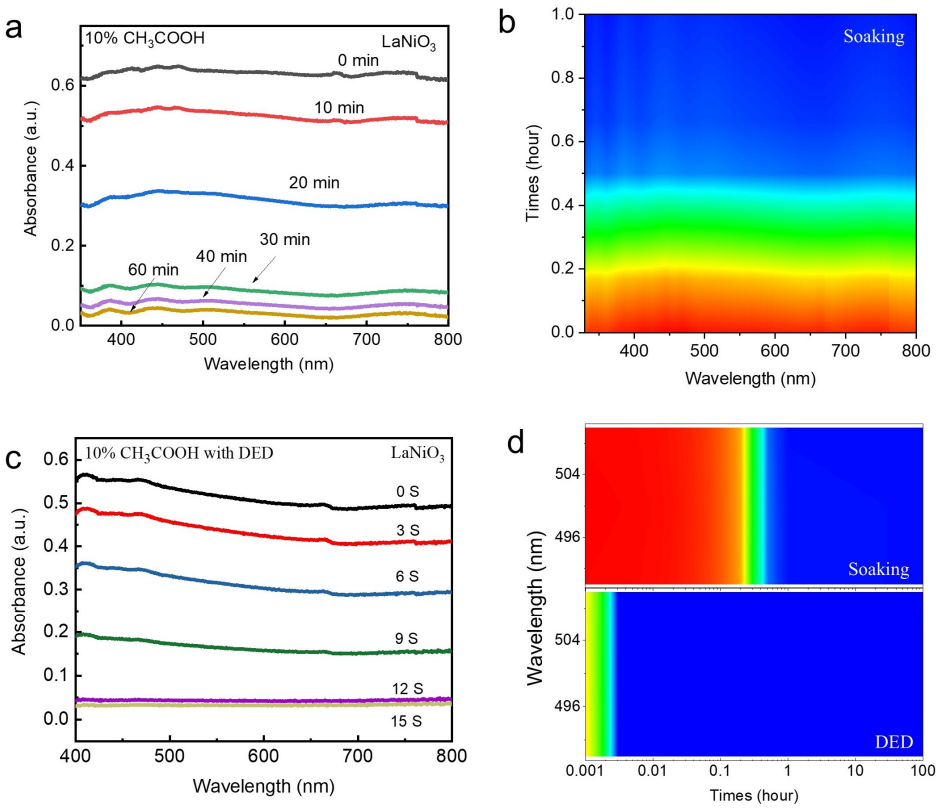

Extended Data Fig. 3 Soaking and Electrodynamic decomposition of the sacrificial layer. The ultraviolet-visible light absorption spectroscopy of (**a**) LNO thin films on LAO substrate in 10% CH_3COOH for various durations. The mapping of time and ultraviolet-visible light absorption spectroscopy of (**b**) LNO on the single LAO substrate after stored in acetic acid. The ultraviolet-visible light absorption spectroscopy of (**c**) LNO thin films on LAO substrate in 10% CH_3COOH through directional electrodynamic decomposition (DED) method for various durations. The mapping of time and ultraviolet-visible light absorption spectroscopy of (**d**) LNO on the single LAO substrate after stored in acetic acid with DED and without DED.

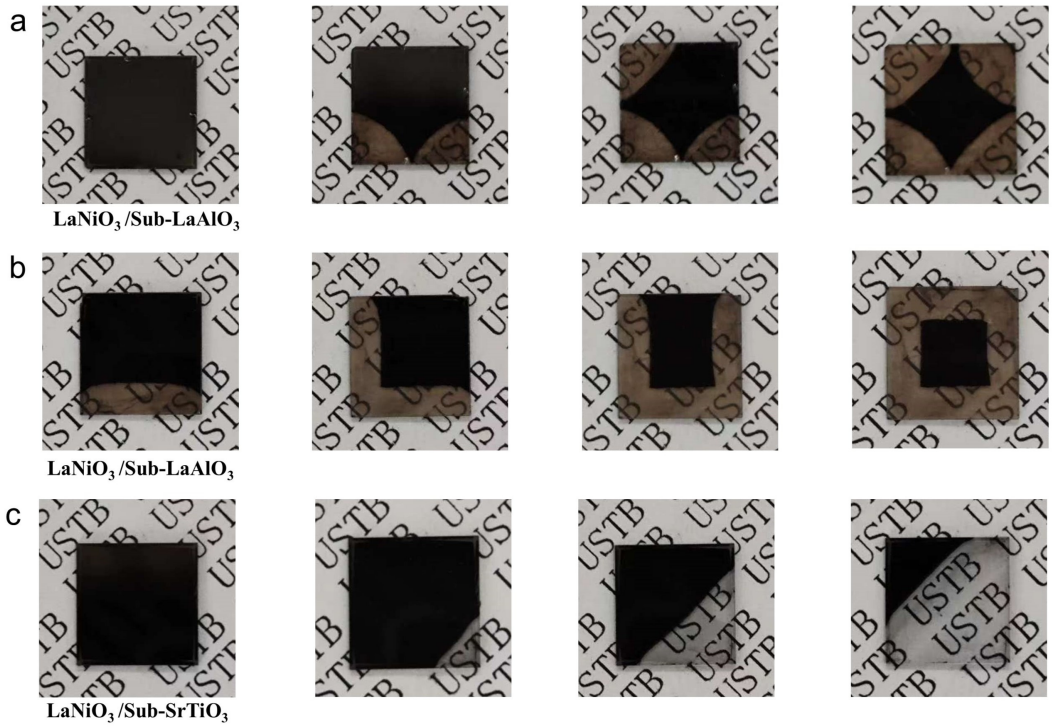

Extended Data Fig. 4 Multi-directivity of DED process. (**a**) Decomposition from the four corners of LNO/LAO sample. (**b**) Decomposition from the four sides of LNO/LAO sample. (**c**) Decomposition from the oblique direction of LNO/STO sample.

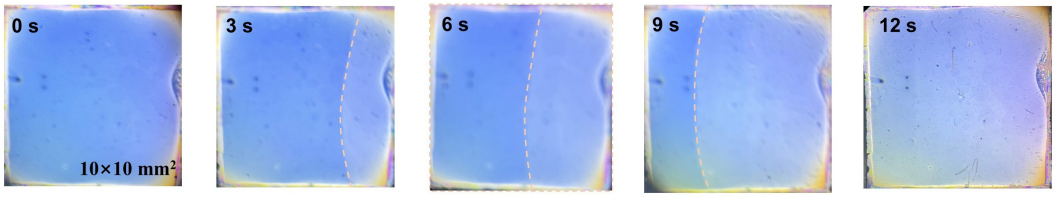

Extended Data Fig. 5 Optical micrographs of 2-nm-thickness sacrificial layers decomposition via DED approach with the target layer of PZO films, indicating the flat and wrinkle-free films.

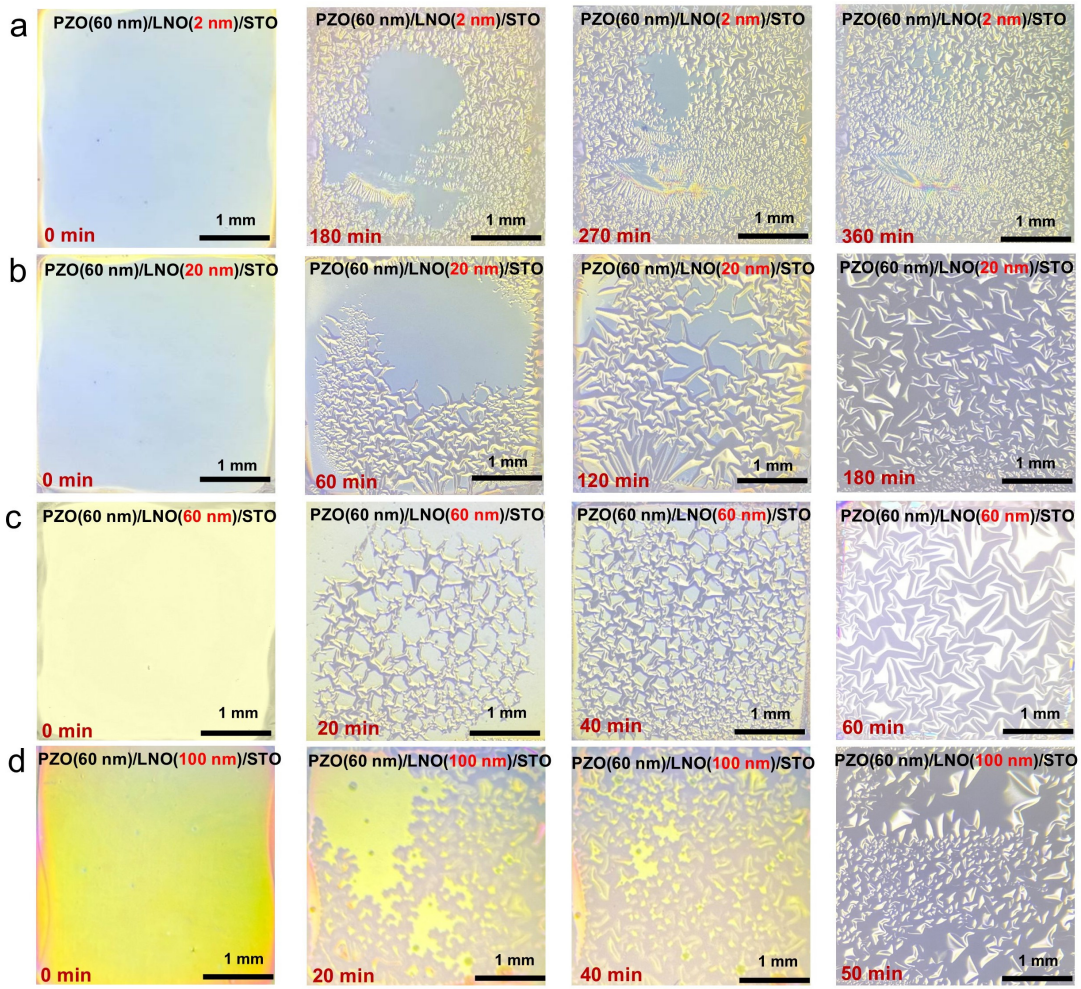

Extended Data Fig. 6 Optical micrographs of different thickness sacrificial layers decomposition via conventional soaking approach with the target layer of PZO films. (**a**) 2-nm-thickness sacrificial layer of LNO. (**b**) 20-nm-thickness sacrificial layer of LNO. (**c**) 60-nm-thickness sacrificial layer of LNO. (**d**) 100-nm-thickness sacrificial layer of LNO, indicating that the thinner the sacrificial layer, the slower the decomposition rate in the conventional soaking approach.

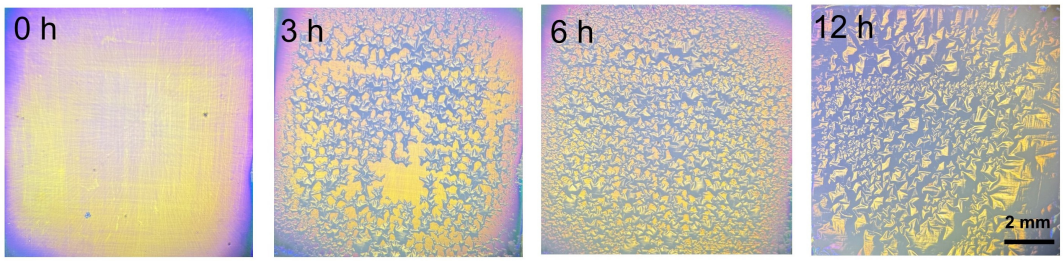

Extended Data Fig. 7 Optical micrographs for conventional soaking decomposition of the 100-nm-thickness LNO/STO (10x10 mm^2) samples. Through the comparison with the small area (Fig. 2d), it shows that in the soaking method, the larger the area size, the slower the decomposition rate.

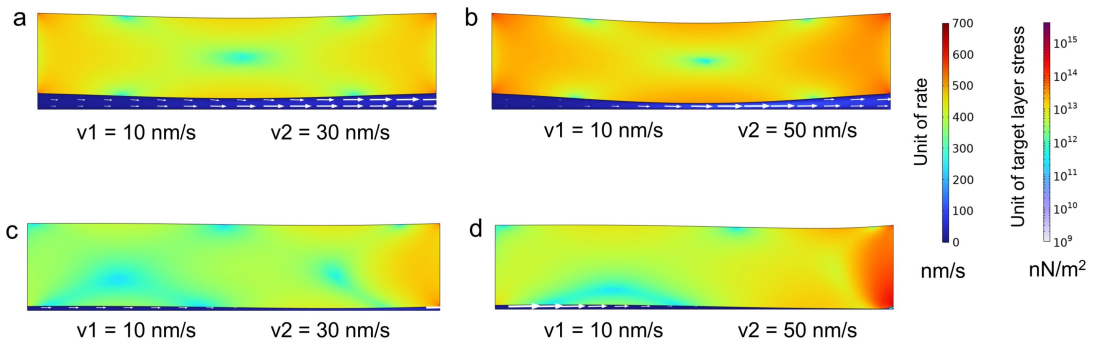

Extended Data Fig. 8 Finite element simulation results of different sacrificial layer thicknesses. (**a**) The target layer stress state of 10 nm/s diffusion velocity and 30 nm/s decomposition velocity with the sacrificial layer thickness of 20 nm. (**b**) The target layer stress state of 10 nm/s diffusion velocity and 50 nm/s decomposition velocity with the sacrificial layer thickness of 20 nm. (**c**) The target layer stress state of 10 nm/s diffusion velocity and 30 nm/s decomposition velocity with the sacrificial layer thickness of 5 nm. (**d**) The target layer stress state of 10 nm/s diffusion velocity and 50 nm/s decomposition velocity with the sacrificial layer thickness of 5 nm.

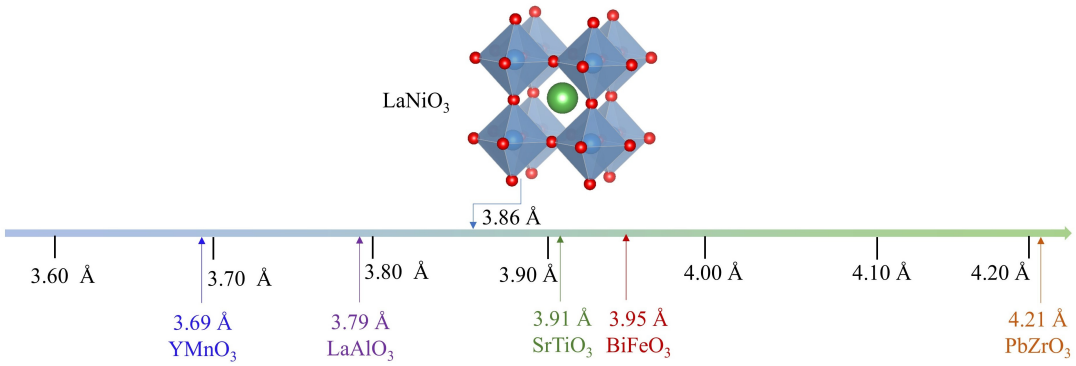

Extended Data Fig. 9 Lattice parameters of LNO sacrificial layer possessing a classical perovskite structure that are perfectly matched to almost perovskite oxides. This versatile sacrificial layer can be effectively matched to the lattice parameters of a wide range of oxide perovskite films, such as the functional materials of $YMnO_3$ (YMO) with a lattice constant of 3.69 Å, $LaAlO_3$ (LAO) with a lattice constant of 3.79 Å, the dielectric material $SrTiO_3$ (STO) with 3.91 Å, the multiferroic material $BiFeO_3$ (BFO) with 3.95 Å, and the antiferroelectric material $PbZrO_3$ (PZO) with 4.21 Å.

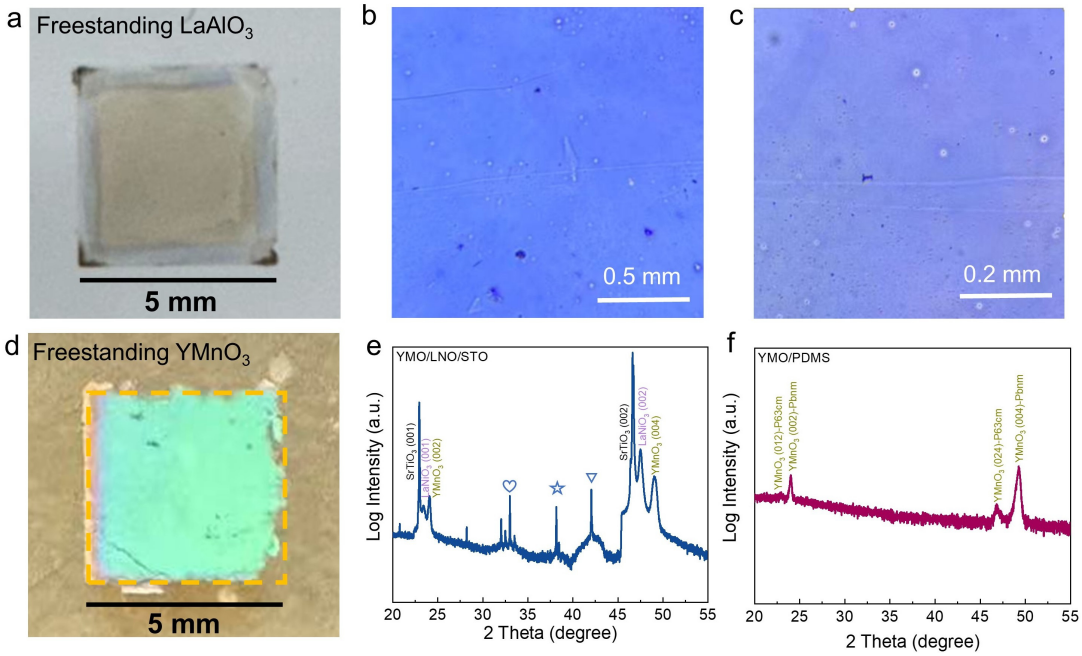

Extended Data Fig. 10 Optical photographs and structures of LAO and YMO freestanding films. (**a-c**) Microphotographs of LAO freestanding films at different magnifications, demonstrating a significant uncracked and flat morphology. (**d**) Microphotographs of YMO freestanding films, displaying a relatively complete flat state, except for some missing on the edges. (**e**) XRD patterns of YMO film grown on STO substrate with LNO sacrificial layer, indicating the high epitaxial grown of YMO with Pbnm structure. The star and triangle marked peaks represent STO (002) plane of Cu-Kβ and W-Lβ rays, respectively, while the heart peaks are from other rays. (**f**) XRD patterns of freestanding YMO film on PDMS. The release of strain may induce a small amount of YMO to transform from Pbmn phase to P63cm phase.

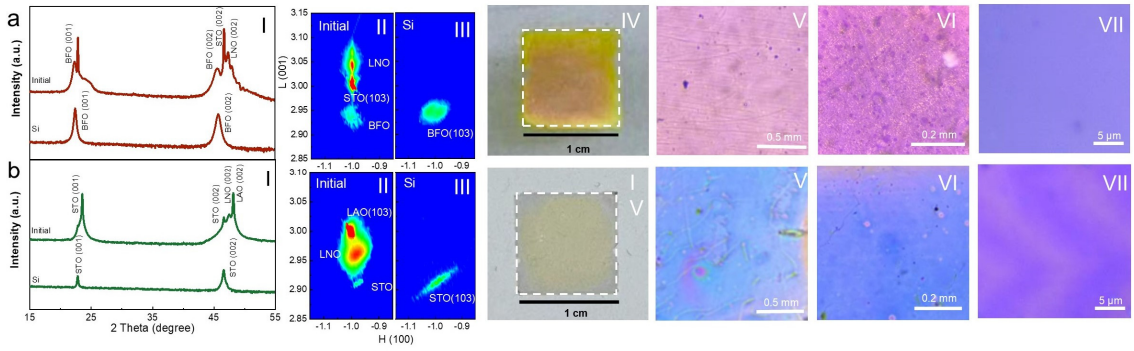

Extended Data Fig. 11 Structure and morphology of the target functional oxide layer. The structure and morphology of (**a**) BFO (magnetron sputtering) and (**b**) STO (sol-gel) epitaxial films before and after stripping. (I) XRD patterns of BFO and STO films before and after stripping. Reciprocal space mapping (RSM) studies of BFO and STO films around (103) peak (II) before and (III) after releasing from the substrate. (IV-VI) Microphotographs of BFO and STO freestanding films at different magnifications, displaying a significant uncracked morphology.

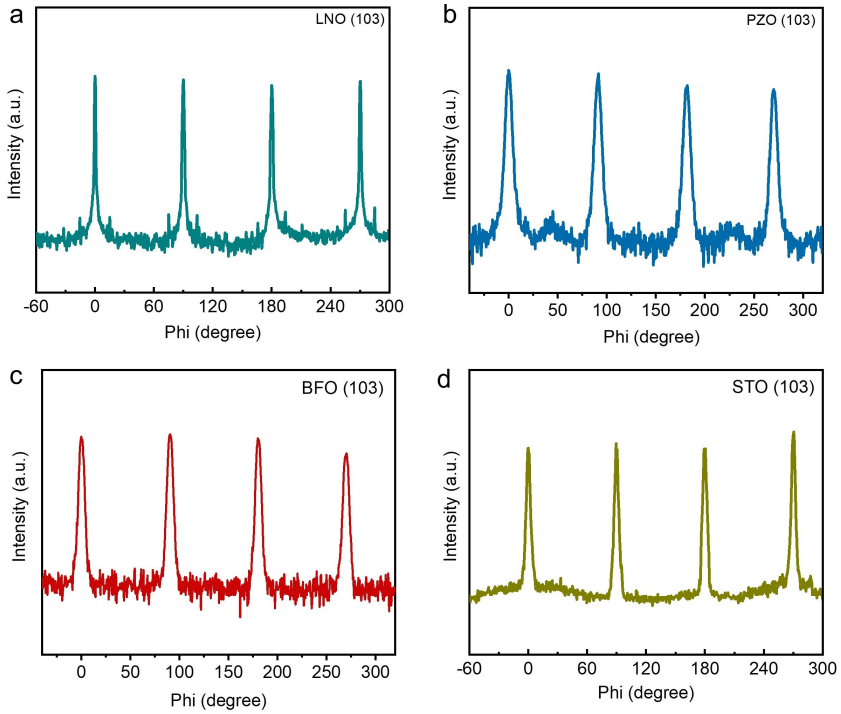

Extended Data Fig. 12 Phi scans of the present thin films. (a) LNO film. **(b)** The freestanding PZO film. **(c)** The freestanding BFO film. **(d)** The freestanding STO film. This indicates the freestanding films remain their original epitaxial properties.

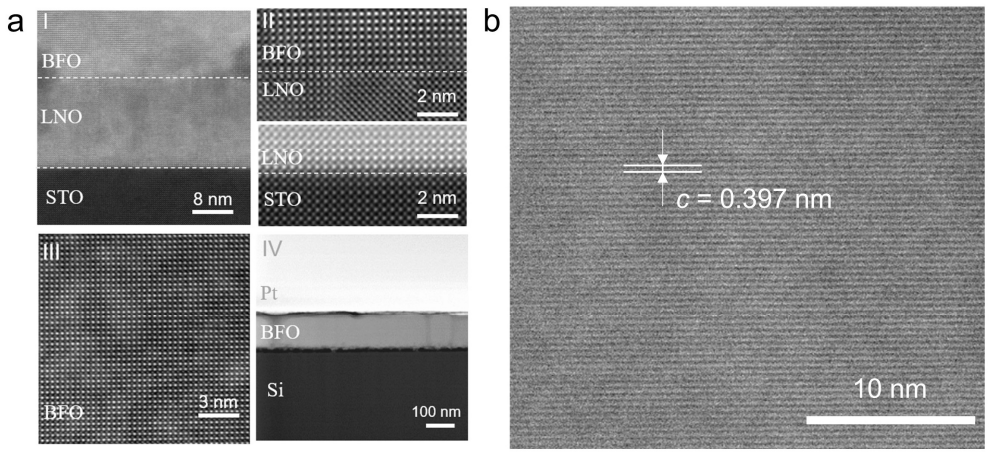

Extended Data Fig. 13 Microstructure of the present BFO film. (**a**) STEM images of (**I-III**) as-grown BFO thin film and (**IV**) freestanding BFO membrane. (**b**) High resolution TEM image of the stripped BFO film.

The as-grown BFO film also exhibits distinct epitaxial growth interfaces and high-crystal quality (Extended Data Fig. 13a-I to 13a-III). The BFO film transferred to Si substrate maintains a high degree of flatness (Extended Data Fig. 13a-IV), along with excellent epitaxial crystallinity. The large areas of (001) lattice fringes can be seen (Extended Data Fig. 13b). As no suitable zone axis of (100) or (010) is found, the lattice of in-plane cannot be obtained.

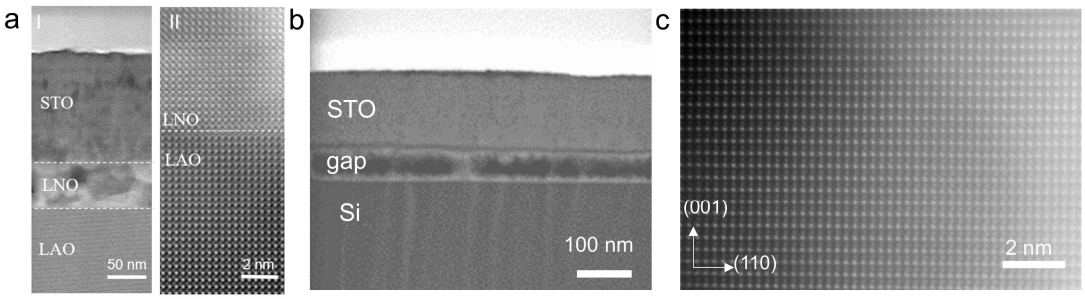

Extended Data Fig. 14 Microstructure of the present STO film. (**a**) STEM images of (**I** and **II**) STO/LNO/LAO structure. (**b**) The cross-section TEM image of the stripped STO film transferred to Si substrate, indicating the relatively flat STO freestanding film. The gap between STO and Si may be caused by surface tension during transfer. (**c**) The STEM image of the STO freestanding film along the zone axis of (-110), showing the high quality of the film after stripping.

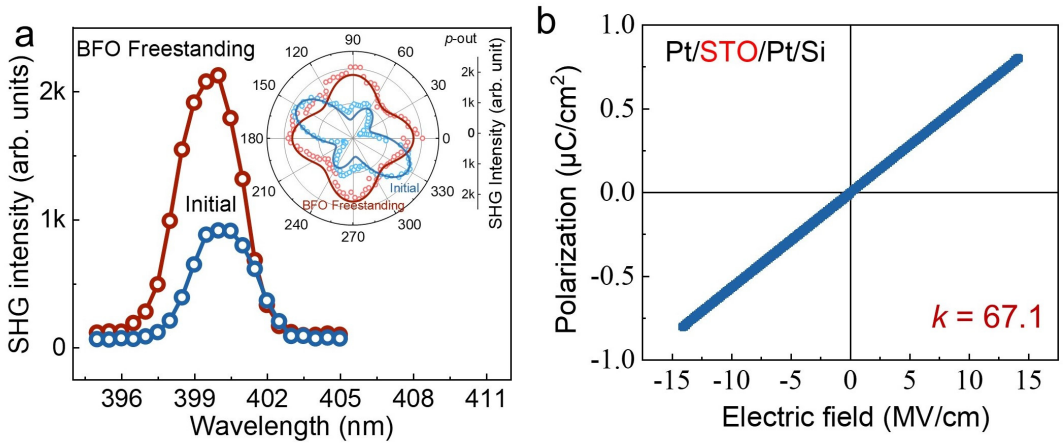

Extended Data Fig. 15 Properties of the present BFO and STO film. (**a**) SHG intensity of BFO as-grown thin film and freestanding membrane. Inset represents their SHG patterns with the *p*-out configurations under polarized light. The scattered points are experimental data, and the lines are fitted based on experimental data. (**b**) Dielectric properties of freestanding STO membrane.

The structure and properties of BFO before and after stripping were characterized by optical second harmonic generation (SHG) testing (Extended Data Fig. 15a). A significant increase in SHG intensity for the freestanding BFO films indicates an enhancement in the ferroelectric signal due to increased spatial inversion symmetry breaking. In the rotational anisotropy SHG measurement, the as-grown BFO film displays two sets of peaks with double rotational symmetry, suggesting the potential presence of twin structures within the film, which may incline towards a monoclinic phase structure (inset of Extended Data Fig. 15a). In contrast, the transferred film demonstrates fourfold symmetry, characteristic of a pseudo-tetragonal BFO phase. The structural transformation in BFO film following stripping is likely associated with the strain release from the LNO sacrificial layer, correlating with the diminished out-of-plane lattice constant observed in XRD and RSM analyses mentioned earlier. Remarkably, the freestanding STO film exhibits an exceptionally high breakdown resistance field of 14 MV/cm and a high dielectric constant of 67.1 (Extended Data Fig. 15b). These properties render the freestanding STO film well-suited for applications in electronic devices.

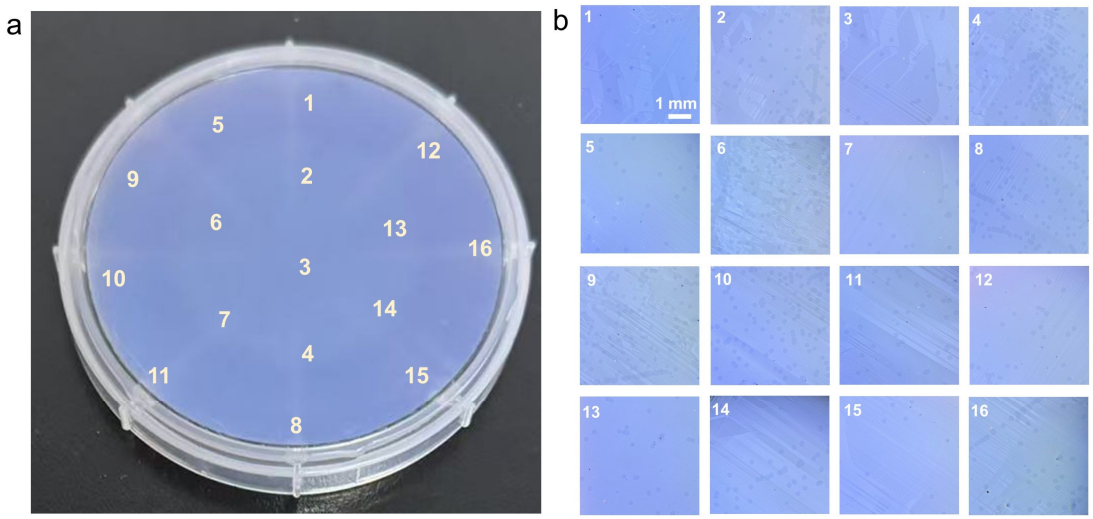

Extended Data Fig. 16 Microphotographs of the 3-inch freestanding membrane. (**a**) Optical photo of the complete 3-inch freestanding PZO film. (**b**) Microphotographs of 16 different regions in Extended Data Fig. 16a, displaying a significant uncracked morphology.

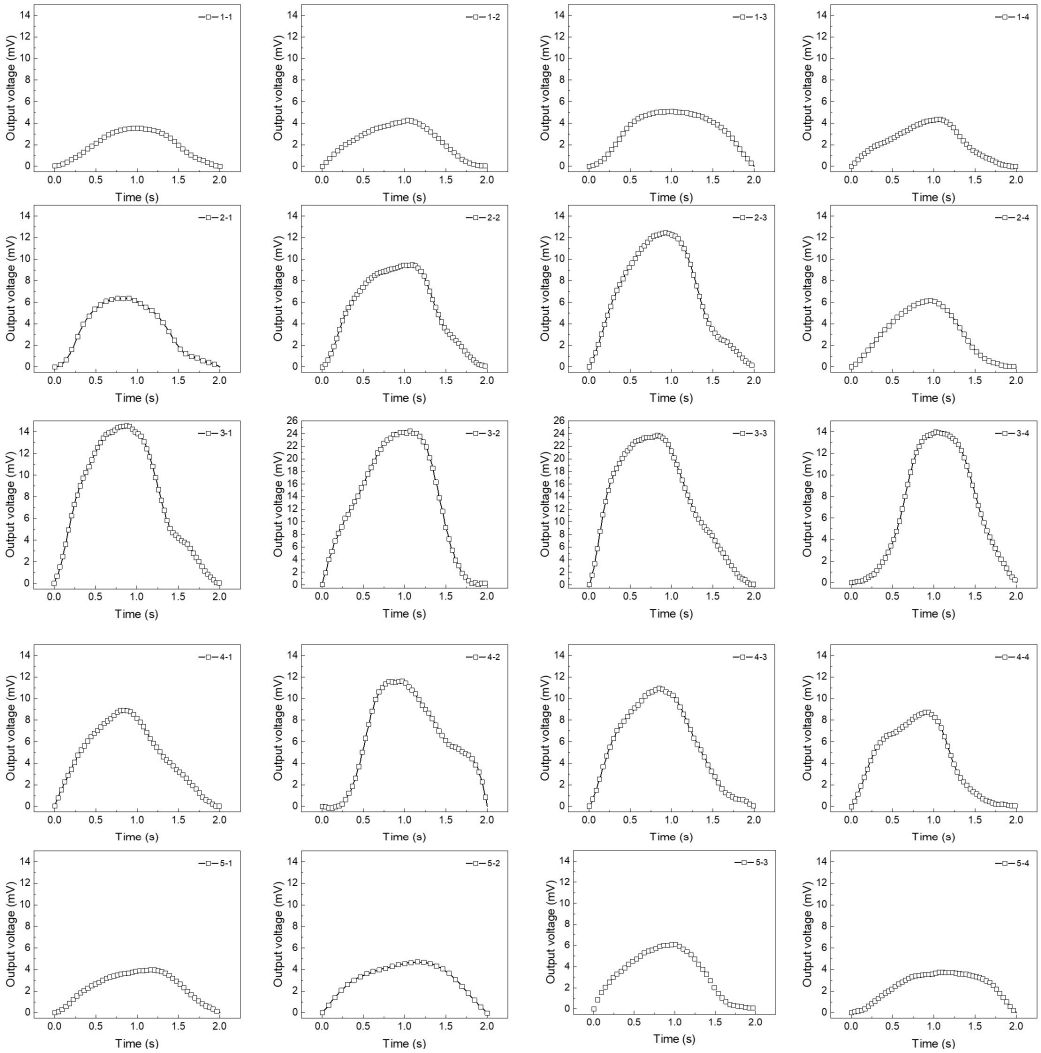

Extended Data Fig. 17 Curves of output voltage and time for the 4×5 piezoelectric sensor array of PZO freestanding film, which is the original data of Fig. 5e.

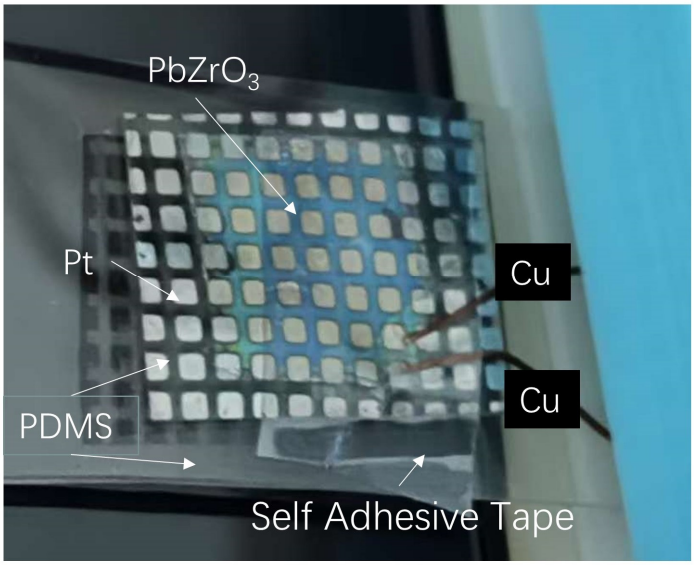

Extended Data Fig. 18 Schematic diagram of the devices used to test the relationship between bending degree and piezoelectric signals

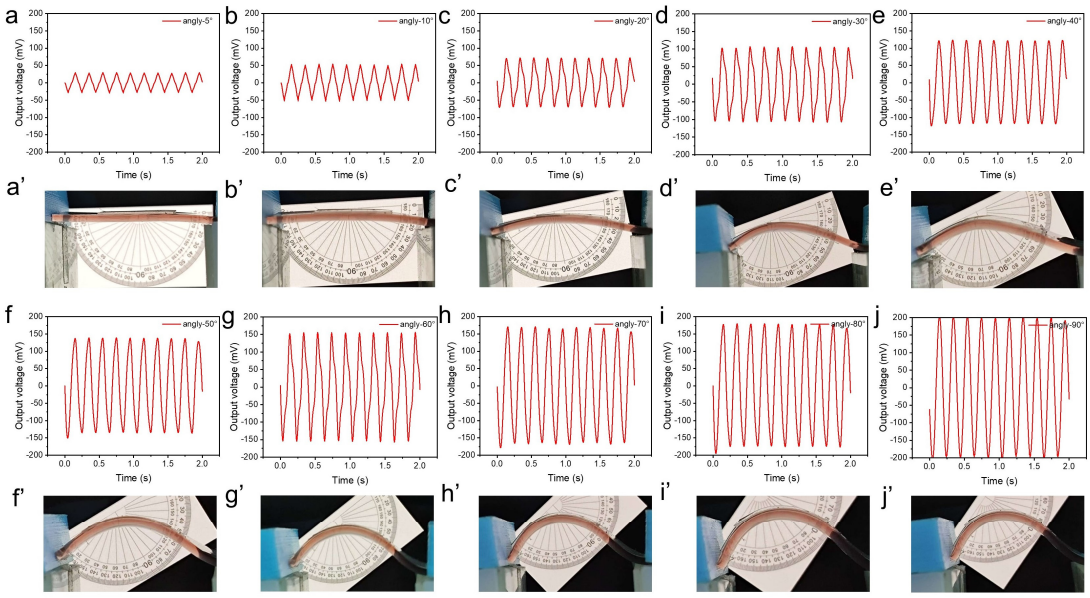

Extended Data Fig. 19 Curves of output voltage and time corresponding to different bending degrees.

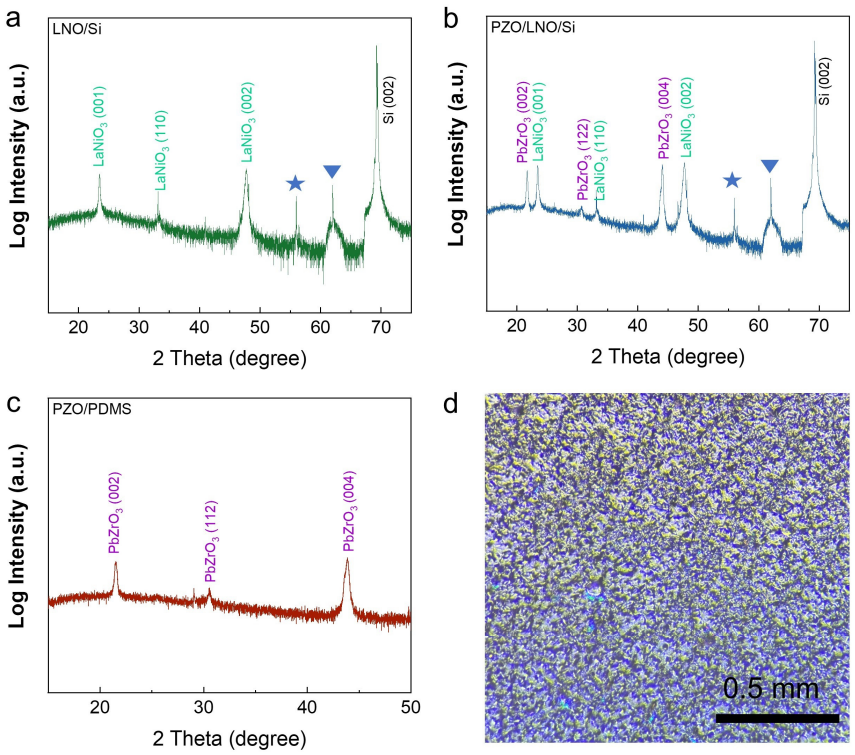

Extended Data Fig. 20 Structure and morphology of the 12-inch film. (**a**) XRD patterns of LNO film grown on Silicon substrate (LNO/Si), indicating the high oriented (00l) direction of LNO. The star and triangle marked peaks represent Si (002) plane of Cu-Kβ and W-Lβ rays, respectively. (**b**) XRD patterns of PZO film grown on LNO/Si, indicating the high oriented (00l) direction of PZO. (**c**) XRD patterns of freestanding PZO film on PDMS, which is consistent with the preferred structure before the stripping. (**d**) Microphotographs of 12-inch PZO freestanding films, displaying a polycrystalline state and significant uncracked morphology.

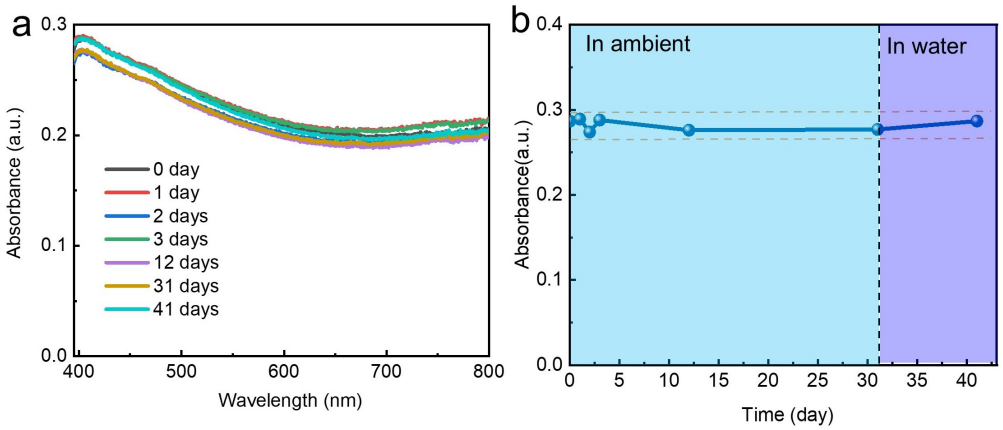

Extended Data Fig. 21 Stability of LNO thin films in ambient and water. (**a**) The ultraviolet-visible light absorption spectroscopy of LNO thin films on STO substrate in ambient (0-31 days) and water (31-41 days). (**b**) The absorption value of 400 nm dependent on the time, indicating the stability of LNO film not only in ambient but also in water. The ambient environment is a temperature of 25 ℃ and a relative humidity of 50%.

Extended Data Table 1 Stripping rate of the traditional soaking method for various sacrificial layers and the DED method for La-based sacrificial layer.

Sacrificial layer	Thickness (nm)	Etching solution	Area/Times	Speed (mm^2/min)	Reference
$La_{0.7}Sr_{0.3}MnO_3$	42	HCl/KI	25 mm^2/36 h	0.012	35
$SrCoO_{2.5}$	10	$Fe(NO_3)$	25 mm^2/3 h	0.14	36
$Sr_3Al_2O_6$	20	Water	25 mm^2/1 h	0.42	23
$SrVO_3$	40	Water	100 mm^2/2 h	0.83	18
SrO	16	Water	25 mm^2/30 min	0.84	37
$Ba_3Al_2O_6$	13.2	Water	25 mm^2/10 min	2.5	38
$YBa_2Cu_3O_{7-x}$	24	HCl	25 mm^2/10 min	2.5	21
$Sr_4Al_2O_7$	20	Water	25 mm^2/6 min	4.2	23
BaO	16	Water	25 mm^2/5 min	5	41
$SrCuO_2$	40	KI	25 mm^2/5 min	5	39
$LaNiO_3$	100	AA	12.3 mm^2/45 min	0.27	This Work
$LaNiO_3$+DED	2	AA	900 mm^2/1.5 min	600	This Work

References

33. G. Kresse, D. Joubert. From ultrasoft pseudopotentials to the projector augmented-wave method. *Phys. Rev. B* **59**, 1758 (1999). doi.org/10.1103/PhysRevB.59.1758

34. J. P. Perdew, K. Burke, M. Ernzerhof. Generalized gradient approximation made simple. *Phys. Rev. Lett.* **77**, 3865 (1996). doi: 10.1103/PhysRevLett.77.3865

35. Y. Shen, K. Ooe, X. Yua, T. Yamada, S. Kobayashi, M. Haruta, D. Kan, Y. Shimakawa. Nat. Commun. 15, 4789 (2024). doi: 10.1038/s41467-024-49055-w

36. W. Zhou, W. Han, Y. Yang, L. Shu, Q. Luo, Y. Ji, C. Jin, Y. Zhang, J. Song, M. Ye, Q. Liu, S. Hu, L. Chen. Synthesis of freestanding perovskite oxide thin films by using brownmillerite $SrCoO_{2.5}$ as a sacrificial layer. *Appl. Phys. Lett.* **122**, 062901 (2023). doi:10.1063/5.0131056

37. S. Varshney, S. Choo, L. Thompson, Z. Yang, J. Shah, J. Wen, S. J. Koester, K. A. Mkhoyan, A. S. McLeod, B, Jalan. Hybrid molecular beam epitaxy for single-crystalline oxide membranes with binary oxide sacrificial layers. *ACS Nano* **18**, 6348–6358 (2024). doi: 10.1021/acsnano.3c11192

38. P. Singh, A. Swartz, D. Lu, S. S. Hong, K. Lee, A, F. Marshall, K. Nishio, Y. Hikita, H. Y. Hwang. Large-area crystalline $BaSnO_3$ membranes with high electron mobilities. *ACS Appl. Electron. Mater.* **1**, 1269–1274 (2019). doi:10.1021/acsaelm.9b00215

39. M. Sheeraz, M.-H. Jung, Y. K. Kim, N.-J. Lee, S. Jeong, J. S. Choi, Y. J. Jo, S. Cho, I. W. Kim, Y.-M. Kim, S. Kim, C. W. Ahn, S. M. Yang, H. Y.g Jeong, T. H. Kim. Freestanding oxide membranes for epitaxial ferroelectric heterojunctions. *ACS Nano* **17**, 13510–13521 (2023). doi: 10.1021/acsnano.3c01974